

References

- [1] F. Ulaby, R.K. Moore, A.K. Fung, "Microwave Remote Sensing. Active and Passive", Vol I: Microwave Remote Sensing Fundamentals and Radiometry, Addison-Wesley Publishing Company, 1981.
- [2] N. Skou, Microwave Radiometer Systems: Design and Analysis, Artech House, 1981, p.121.
- [3] R. Villarino, L. Enrique, A. Camps, I. Corbella and S. Blanch, "Design, implementation and test of the UPC L-band AUtomatic RAdiometer," Open Symposium on Propagation and Remote Sensing URSI- F 2002, Garmisch-Partenkirchen, Germany, February 2002.
- [4] N. Skou, Microwave Radiometer Systems: Design and Analysis, Artech House, 1981, p. 83
- [5] A. Sumpsi, "Design, implementation and test of a Doppler delay-radiometer," Final Project, ETSETB Polytechnic University of Catalonia, March 2003.
- [6] X. Corominas, "Disseny i implementació d'un radiòmetre polarimètric en banda L: circuits de RF i detecció," Final Project, ETSETB Polytechnic University of Catalonia, January 2001.
- [7] I. Corbella and J. Bará. "A New Structure of Coupled Transmission Line Filters." 30th European Microwave Conference EuMC. Paris 2-6 October 2000. Volume 2 pages 60-62.
- [8] I. Sanz, "Diseño de VCO para aplicaciones MVDS," Final Project, ETSETB Polytechnic University of Catalonia, 2001.
- [9] J. Farré, N. Pizarro, "Optimització de circuits per a un radiometre de banda L," Final Project, ETSETB Polytechnic University of Catalonia, January 2002
- [10] J. Capdevila, "Design and Implementation of an X-band Polarimetric Radiometer," Final Project, ETSETB Polytechnic University of Catalonia, January 1998.
- [11] S. Franco, Design With Operational Amplifiers and Analog Integrated Circuits, McGraw-Hill International Editions, USA, 1988 , pp.372.
- [12] F.J. Monzón, "Implementación de un correlador digital de alta velocidad en PLD", Final Project, Polytechnic University of Catalonia, July 1998.
- [13] R. Villarino, "Manual del experimento del radiómetro LAURA," Internal publication, Polytechnic University of Catalonia, July 2002.
- [14] R. Villarino, "Radiómetro polarimétrico en Banda X: diseño de las antenas, control de temperatura y estructura mecánica," Final Project, ETSETB Polytechnic University of Catalonia, January 2000.
- [15] L. Enrique, "Manual de software del radiómetro LAURA," Internal publication, Polytechnic University of Catalonia, July 2002.Internal Publication.

- [16] UNESCO technical papers in marine science. Background papers and supporting data on the Practical Salinity Scale, 1978. Num 37, p141-144.
- [17] D. Weaire, S. Hutzler, "The Physics of Foams", Clarendon press, Oxford 1999. Reich, W., 1982, A radio continuum survey of the northern sky at 1420 MHz – Part I, Astron- Astrophys. Suppl. Ser., 48, 219-297.
- [18] P. Reich, and W. Reich, 1986, A radio continuum survey of the northern sky at 1420 MHz – Part I, Astron- Astrophys. Suppl. Ser., 63, 205-292.
- [19] A. Camps, I. Corbella, J. Font, J. Etcheto, V. Caselles, and A. Weill, "WISE 2000 and 2001: Campaign Description And Executive Summary", *Proceedings of the First Results Workshop on WISE/LOSAC/EuroSTARSS Campaigns*, ESA, pp. 17-26, France, 4-6 Nov 2002.
- [20] A. Camps, R. Villarino, L. Enrique, M. Vall-llossera, J. Miranda, I. Corbella, "Sea Surface Emissivity At L-Band: Derived Dependence With Incidence And Azimuth Angles", *Proceedings of the First Results Workshop on WISE/LOSAC/EuroSTARSS Campaigns*, ESA, pp. 105-106, France, 4-6 Nov 2002.
- [21] A. Camps, et al. "Wind and Salinity Experiment 2000, Experiment Plan", May 2000.
- [22] A. Camps, et al. "Wind and Salinity Experiment 2001, Experiment Plan", October 2001.
- [23] "Wind and Salinity Experiment 2000, Data Acquisition Report, Version 1.0", May 2001
- [24] J. Guo, L. Tsang, W. Asher, K.-H. Ding and C.-T. Chen, " Applications of dense media radiative transfer theory for passive microwave remote sensing of foam covered ocean", IEEE Transactions Geoscience and Remote Sensing, Vol. 39, No. 5, pp. 1019-1027, May 2001.
- [25] N. Reul, N, and B. Chapron, " Effects of foam on the emissivity of the sea surface at L-band, WP 1300 Report, ESA contract N° 15165/01/NL/SF April 2001.
- [26] A. Guissard, "Atmospheric instability above the ocean and implications for scatterometry", submitted for publication December 2001.
- [27] L.A. Klein and C.T. Swift, "An Improved Model for the Dielectric Constant of Sea Water at Microwave Frequencies", IEEE Journal of Oceanic Engineering, OE-Vol 2, No 1, pp 104-111, 1977.
- [28] J. P. Hollinger, "Passive microwave measurements of sea surface roughness," *IEEE Trans. Geosci. Electron.*, vol. GE-9, no. 3, pp. 165–169, 1971.
- [29] F. Ulaby, R. Moore, A. Fung "Microwave Remote Sensing: Active and Passive- Volume III: Active Microwave Sensing of the Ocean". Artech House, 1986, pp. 1653.
- [30] C.T. Swift, "Microwave Radiometer Measurements of the Cape Cod Canal", Radio Science, Vol. 9, No. 7, pp 641-653, 1974.

- [31] S.H. Yueh, "Modeling of Wind Direction Signals in Polarimetric Sea Surface Brightness Temperatures", *IEEE Transactions on Geoscience and Remote Sensing*, Vol. 35, No 6, November 1997.
- [32] M. Vall-llossera, J. Miranda, A. Camps, and R. Villarino, "Sea Surface Emissivity Modelling at L-band: An Inter-comparison Study", *Proceedings of the First Results Workshop on WISE/LOSAC/EuroSTARSS Campaigns*, ESA, pp. 143-153, France, 4-6 Nov 2002.
- [33] T. Elfouhaily, B. Chapron, K. Katsaros, and D. Vandemark, "A Unified Directional Spectrum for Long and Short Wind-driven Waves," *Journal of Geophysical Research*, Vol. 102, pp. 15781-15796, 1997.
- [34] S.L. Durden, and J. F. Vesely, "A Physical Radar Cross-Section Model for a Wind-Driven Sea with Swell," *IEEE Journal Of Oceanic Engineering*, Vol. OE-10, pp. 445-451, 1985.
- [35] A. Camps, and S.C. Reising, "A Model for Wind Direction Signature in the Stokes Emission Vector of the Ocean Surface at Microwave Frequencies", *Microwave and Optical Technology Letters*, Vol. 29(6), pp. 426-432, June 2001.
- [36] R. Villarino, A. Camps, M. Vall-llossera, J. Miranda, and J. Arenas, "Sea foam and sea state effects on the instantaneous brightness temperatures at L-band", *Proceedings of the First Results Workshop on WISE/LOSAC/EuroSTARSS Campaigns*, ESA, pp. 95-103, France, 4-6 Nov 2002.
- [37] F. Ulaby, R.K. Moore, A.K. Fung, "Microwave Remote Sensing. Active and Passive", Vol III, Artech House, 1986.
- [38] E.C. Monahan, and I. Muircheartaigh, "Whitecaps and the passive remote sensing of the ocean surface", *Int. J. Remote Sensing*, Vol. 7, No. 5, pp. 627-642, 1986.
- [39] E.C. Monahan, and M. Lu, "Acoustically Relevant Bubble Assemblages and Their Dependence on Meteorological Parameters", *IEEE Journal Of Oceanic Engineering*, Vol. 15, No. 4, October 1990.
- [40] E.C. Monahan, "Whitecap coverage as a monitorable indication of the rate of bubble injection into oceanic mixed layer. Sea Surface Sound", Dordrecht, the Netherlands: Kluwer academic Publisher, 1988.
- [41] E.C. Monahan, "Occurrence and evolution of acoustically relevant subsurface bubble plumes and their associated, remotely monitorable, surface whitecaps. Natural Physical Sources of underwater sounds: Sea Surface Sound (2)", Dordrecht, the Netherlands: Kluwer academic Publisher, 1993.
- [42] I.V. Cherny and V. Y. Raizer, *Passive Microwave Remote Sensing of Oceans*. Wiley-Praxis Series in Remote Sensing, 1998. 193 pages.
- [43] G.S. Bordonskiy, I. B. Vasil'kova, N. N. V. V. M. Veselov, Y. A. Miliitskiy, V. G. Mirovskiy, V. N. Nkitin, V. Y. Raizer, Y. B. Khapin, Y. A. Sharkov, and V. S. Etkin, "Spectral characteristics of the

- emissivity of foam formations," Izvestiya, Atmospheric and Oceanic Physics, vol. 14, no. 6, pp. 464-469, 1978.
- [44] E.C. Monahan and D. K. Woolf, "Comments on variations of whitecap coverage with windstress and water temperature," J. Phys. Oceanogr., vol. 19, pp. 706-709, 1989.
- [45] C. Reising, K. A. Horgan and M. A. Aziz, "Passive polarimetric Remote Sensing of the Ocean Surface: The Effect of Surface Roughness and Whitecaps", URSI General Assembly '02 Maastricht, Netherlands, August 2002.
- [46] M.A. Donelan, and Pierson, W. J., "Bragg-scattering and equilibrium ranges in wind-generated waves, with application to scatterometry ", J. Geophys. Res., 1985.
- [47] C. Craeye, Sobieski, P.W., and Bliven, L.F., "Scattering by artificial wind and rain roughened water surfaces at oblique incidences", Int. J. Remote Sensing, Vol 18, No 10, pp 2241-2246, 1997.
- [48] W. Reich, 1982, A radio continuum survey of the northern sky at 1420 MHz – Part I, Astron-Astrophys. Suppl. Ser., 48, 219-297.
- [49] J. Arenas, "Determinación de parámetros de la espuma del mar con aplicaciones en teledetección," Final Project, EUPBL Polytechnic University of Catalonia, September 2001.
- [50] J. Miranda, M. Vall-llossera, R. Villarino, A. Camps, "Sea state and rain effects in the sea surface emissivity at L-Band", *Proceedings of the First Results Workshop on WISE/LOSAC/EuroSTARSS Campaigns*, ESA SP 525, pp. 17-26, France, 4-6 Nov 2002.
- [51] J. Miranda, M. Vall-llossera, R. Villarino, A. Camps, "Sea state and rain effects in the sea surface emissivity at L-Band", *Proceedings of the First Results Workshop on WISE/LOSAC/EuroSTARSS Campaigns*, ESA SP 525, pp. 17-26, France, 4-6 Nov 2002.

Publications

Journal Papers.

1. Camps A., J.Font, J. Etchetto, V. Caselles, A. Weill, I. Corbella, M. Vall-llossera, N. Duffo, F. Torres, **R. Villarino**, L. Enrique, A. Julià, C. Gabarró, J. Boutin, E. Rubio, S.C. Reising, P. Wursteisen, M. Berger, M. Martín-Neira. "Sea Surface Emissivity Observations at L-band: First Results of the Wind and Salinity Experiment WISE 2000". IEEE Transactions on Geoscience and Remote Sensing, Vol 40, No 10, October 2002, pp 2117-2130.

2. A. Camps, J. Font, M. Vall-llossera, C. Gabarró, I. Corbella, N. Duffo, F. Torres, S. Blanch, A. Aguasca, **R. Villarino**, L. Enrique, J. Miranda, J. Arenas, A. Julià, J. Etchetto, V. Caselles, A. Weill, J. Boutin, S. Contardo, R. Niclós, R. Rivas, S.C.Reising, P. Wursteisen, M. Berger, and M. Martín-Neira, "The *WISE* 2000 and 2001 campaigns in support of the SMOS Mission: Sea Surface L-Band Brightness Temperature Observations And Their Application to Multi-Angular Salinity Retrieval". IEEE Transactions on Geoscience Remote Sensing, Vol 42 No 4, April 2004, pp 804 a 823.

3. Camps, A., I. Corbella, M. Vall-llossera, N. Duffo, F. Torres, **R. Villarino**, L. Enrique , F. Julbé, J. Font, A. Julià, C. Gabarró, J. Etchetto, J. Boutin, A. Weill, V. Caselles, E. Rubio, P. Wursteisen, M. Martín-Neira. "L-band Sea Surface Emissivity: Preliminary Results of The WISE-2000 Campaign And its Application to Salinity Retrieval in The SMOS Mission". Radio Science Volumen: 38, No. 4, 8071, 10.1029/2002RS002629, June 2003.

4. A. Camps, M. Vall.llossera, **R. Villarino**, R. Rodríguez, R. Sabia, A. Monerris, I. Corbella, N. Duffo, F. Torres, "Foam –covered and rain-roughned sea surface emissivity at L-band: Results from the FROG 2003 experiment ". 8th specialist meeting on microwave radiometry and remote sensing applications, Rome, February 2004, IEEE Transactions on Geoscience Remote Sensing, special issue submitted for publication.

Conferences and workshop proceedings.

5. Camps A., I. Corbella, M. Vall-llossera, **R. Villarino**, L. Enrique, J. Font, A. Julià, C. Gabarró, J. Etchetto, J. Boutin, A. Weill, F. Torres, N. Duffo, R. Niclós, V. Caselles, P. Wursteinsen y M. Martín-Neira." Sea Surface Emissivity Observations at L-band: First Preliminary Results of the Wind and Salinity Experiment WISE 2000". International Geoscience ad Remote Science Symposium, IGARSS '01, Sydney (Australia), July 2001.

6. Camps A., I. Corbella, M. Vall-llossera, **R. Villarino**, L. Enrique, , F. Julb , J. Font, A. Juli , C. Gabarr , J. Etchetto, J. Boutin, A. Weill, N. Duffo, F. Torres, V. Caselles, E. Rubio, P. Wursteinsein y M. Mart n-Neira. " L-band sea surface emissivity: preliminary results of The WISE 2000 campaign and its application to salinity retrieval in the SMOS mission". Microrad '01 conference. Boulder (Colorado), USA, November 2001.
7. **Villarino R.**, L. Enrique, A. Camps, I. Corbella y S. Blanch. "Design, implementation and test of the UPC L-band AUtomatic RAdiometer". Open Symposium on Propagation and Remote Sensing URSI- F 2002, Garmisch-Partenkirchen, February 2002.
8. Camps A., I. Corbella, M. Vall-llossera, F. Torres, N. Duffo, **R. Villarino**, L. Enrique, J. Miranda, J. Arenas, J. Font, A. Juli , C. Gabarr , J. Etchetto, J. Boutin, S. Contardo, A. Weill, R. Nicl s, V. Caselles, P. Wursteisen, M. Berger y M. Mart n-Neira. "Wind Effects on the Sea Surface Emissivity at L-band: Preliminary Results of WISE 2000 and 2001". Open Symposium on Propagation and Remote Sensing URSI- F 2002, Garmisch-Partenkirchen, February 2002.
9. Camps A., J. Font, J. Etchetto, A. Weill, V. Caselles, I. Corbella, M. Vall-llossera, F. Torres, N. Duffo, **R. Villarino**, L. Enrique, J. Miranda, A. Juli , C. Gabarr , J. Boutin, R. Nicl s, P. Wursteisen, M. Berger y M. Mart n-Neira. "L-band Sea Surface Emissivity Radiometric Observations under High Winds: Preliminary Results of the Wind ad Salinity Experiment WISE-2001". International Geoscience ad Remote Sensing Symposium, IGARSS '02. Toronto (Canada), June 2002.
10. Camps A., J. Font, J. Etchetto, ,V. Caselles, I. Corbella, M. Vall-llossera, F. Torres, N. Duffo, **R. Villarino**, L. Enrique, J. Miranda, J. Arenas, A. Juli , C. Gabarr , J. Boutin, S. Contardo, A. Weill, R. Nicl s, R. Rivas, S.C. Reising, P. Wursteisen, M. Berger y M. Mart n-Neira. "Sea Surface Radiometric Observations At L-band: Wind Speed Sensitivity Derived From WISE 2000 and 2001". Proceedings of the URSI General Assembly (CD-ROM). Maastrich, The Netherlands, August 2002.
11. **R. Villarino**, A. Camps, M. Vall-llossera, J. Miranda, J. Arenas, "Sea Foam And Sea State Effects On The Instantaneous Brightness Temperatures At L-Band". EuroSTARRS, WISE and LOSAC, ESA Publications Division (ISBN 92-9092-835-2), pp (95 a 103), November 2002.

12. A. Camps, **R. Villarino**, L. Enrique, M. Vall-llossera, J. Miranda, I. Corbella, "Sea Surface Emissivity at L-Band: Derived Dependence with Incidence and Azimuth Angles". EuroSTARRS, WISE and LOSAC, ESA Publications Division (ISBN 92-9092-835-2), pp (105 a 116), November 2002.
13. M. Vall-llossera, J. Miranda, A. Camps, **R. Villarino**, "Sea Surface Emissivity Modelling at L-Band: An Inter-Comparison Study". EuroSTARRS, WISE and LOSAC, ESA Publications Division (ISBN 92-9092-835-2), pp (143 a 153), November 2002.
14. J. Miranda, M. Vall-llossera, **R. Villarino**, A. Camps, "Sea State and Rain Effects on Sea Surface Emissivity at L-Band". EuroSTARRS, WISE and LOSAC, ESA Publications Division (ISBN 92-9092-835-2), pp (155 a 162), November 2002.
15. A. Camps, M. Vall-llossera, **R. Villarino**, J. Miranda, F. Fulbé, B. Vallespín, "Sea Surface Retrieval in the SMOS Configuration: Simulation Performance Study". EuroSTARRS, WISE and LOSAC, ESA Publications Division (ISBN 92-9092-835-2), pp (173 a 180), November 2002.
16. J. Miranda, M. Vall-llossera, A. Camps, **R. Villarino**, "Estimation of Sea Surface Spectrum Under Non-Stationary Conditions". International Geoscience and Remote Sensing Symposium IGARSS 2003. Proceedings of the International Geoscience and Remote Sensing Symposium IGARSS 2003 (CD-ROM), Tolouse France, July 2003.
17. M. Vall-llossera, J. Miranda, A. Camps, **R. Villarino**, N. Duffo, I. Corbella, "Inter-Comparison Study of Asymptotic Models for Sea Surface Emissivity Simulation at L-band". International Geoscience and Remote Sensing Symposium IGARSS 2003. Proceedings of the International Geoscience and Remote Sensing Symposium IGARSS 2003 (CD-ROM), Tolouse France, July 2003.
18. **R. Villarino**, A. Camps, M. Vall-llossera, J. Miranda, J. Arenas, "Sea Foam Effects On The Brightness Temperature At L-Band". International Geoscience and Remote Sensing Symposium IGARSS 2003. Proceedings of the International Geoscience and Remote Sensing Symposium IGARSS 2003 (CD-ROM), Tolouse France, July 2003.
19. **R. Villarino**, A. Camps, I. Corbella, M. Vall-llossera, N. Duffo, F. Torres, L. Enrique, J. Miranda, J. Arenas, J. Font, A. Julià, C. Gabarró, J. Echetto, J. Boutin, S. Contardo, A. Weill, E. Rubio, R.

- Niclós, R. Rivas, V. Caselles, P. Wurteleisen, M. Berger, and M. Martín Neira. "Sea Surface emissivity at L-band. Results of the WInd and Salinity Experiments WISE 2000 and 2001". SPIE's 10th International Symposium on Remote Sensing, Vol 5233, pp (296-307), September 2003.
20. J. Miranda, M. Vall-llossera, A. Camps, **R. Villarino**. "Estimation of sea surface spectrum using neural networks". SPIE's 10th International Symposium on Remote Sensing, Vol 5233, págs (108-117), September 2003.
21. **R. Villarino**, A. Camps, M. Vall-llossera, J. Miranda, R. Sabia, A. Monerris, R. Rodríguez, F. Campoy, J. Fernández, I. Corbella, N. Duffo, F. Torres, J. Arenas, "Sea surface emission at L-band results from the WISE/FROG field experiments ". International Geoscience and Remote Sensing Symposium IGARSS 2004, Anchorage, Alaska, September 2004. Accepted.

List of figures

Figure 1.1. Geometry of the radiation incident over the antenna [1].	2
Figure 1.2. Planck's radiation law [1].	3
Figure 1.3. Comparison of Planck's law with its low-frequency (Rayleigh-Jeans law) and high-frequency (Wien's law) approximations at 300 K.	4
Figure 1.4. The power delivered by: (a) an antenna placed inside of a black-body enclosure of temperature T is equal to the power delivered by (b) a resistor maintained at the same physical T (assuming each one is connected to a matched receiver of bandwidth B).	5
Figure 1.5. Relationship between the antenna temperature T_A , the apparent temperature T_{AP} and the brightness temperature T_B [1].	6
Figure 1.6. (a) SSS Levitus '94 map, and (b) SMOS artist's view.	8
Figure 1.7. Nadir brightness temperature dependence with SSS and SST at 1.4 GHz.	9
Figure 1.8. (a) Location of the Casablanca oil rig and IRTA facilities, (b) Casablanca oil rig (WISE), (c) radiometric measurements (LAURA), and foam generation (FROG), and (d) rain generation (FROG).	9
 Figure 2.1. LAURA electronics [4].	11
Figure 2.2. Block diagram of LAURA [4].	12
Figure 2.3. Functional block diagram of a DR [5].	12
Figure 2.4. Importance of high antenna main beam efficiency: antenna measuring an ice floe [6].	14
Figure 2.5. (a) Antenna aspect, and (b) radiating element.	15
Figure 2.6. (a) Feed network, and (b) antenna's rear view.	15
Figure 2.7. Normalized antenna radiation pattern, (a) co-polar, and (b) cross-polar.	16
Figure 2.8. (a) co-polar cut at E plane, (b) co-polar cut at H plane, (c) cross-polar cut at 45° , and (d) Main Beam Efficiency computed from 0° to θ , and ϕ from 0° to 360° . Secondary lobe level at $\theta = 22^\circ$	16
Figure 2.9. Switch's circuitry, [8].	17
Figure 2.10. (a) MAX2640 matched network [7], and (b) Dicke switch and LNA.	18
Figure 2.11. Band pass filters [9].	18
Figure 2.12. Filter's insertion loss and frequency response, (a) H- channel, and (b) V- channel.	19
Figure 2.13. (a) Down-convert modules (H- and V- channel), and (b) MAR-6 SM connection, [7].	19
Figure 2.14. Frequency response of the downconverter measured with noise thermal, a) H- and b) V- channel.	20
Figure 2.15. (a) Local oscillator, and (b) its phase noise.	20
Figure 2.16. Resistive power splitter.	21
Figure 2.17. Post-detection circuit, (a) picture, and (b) block diagram.	21
Figure 2.18. (a) Video amplifier schematic, and (b) power detector block, [12].	22
Figure 2.19. (a) Differential detector: V_{OUT} vs P_{IN} curve, and (b) linear range in the differential detector, [12].	22
Figure 2.20. Digital correlator radiometer, (a) circuit board, and (b) schematic block diagram.	25
Figure 2.21. (a) Signal conditioning circuitry, and (b) clinometer view.	26
Figure 2.22. (a) PicoLog ADC-16, and (b) voltage to current converter unit module.	26
Figure 2.23. Control Unit.	27
Figure 2.24. Motor controllers.	28
Figure 2.25. LAURA's control temperature instrument. (a) General aspect, (b) front view, and (c) rear view.	29
Figure 2.26. Temperature control module (a) view, and (b) block diagram.	30
Figure 2.27. Switching supply module, (a) view, and (b) block diagram.	31

Figure 2.28. Radiometer rear view aspect, showing the 8 TEC modules temperature to heat/cool the radiometer ...	32
Figure 2.29. (a) Instantaneous reference load temperature and, (b) instantaneous external temperature of the WISE field experiment.....	32
Figure 2.30. Blocks diagram of the basic control system. Block $G_c(s)$ is the control System, $G(s)$ is the system to be controlled, and $H(s)$ the sensors.....	33
Figure 2.31. (a) Digital to analog converter board to connect to the 8255 I/O card, prepared to be install on a ISA bus socket, and (b) circuitry to switch the analogical and the software temperature control.....	35
Figure 2.32. Instantaneous reference load temperature (a) FROG field experiment and, (b) hot load measurement and, instantaneous external temperature (c) the FROG field experiment and, (d) hot load measurement.....	36
Figure 2.33. Industrial PC, (a) front view, and (b) rear view.....	37
Figure 2.34. Current to voltage converters, (a) digital correlator signals, and (b) PicoLog ADC-16.....	37
Figure 2.35. LAURA radiometer mounted on the pedestal, (a) at UPC facilities during testing, and (b) at the Casablanca oil rig during WISE 2001.....	38
Figure 2.36. Radiometer movement system, (a) elevation motor, and (b) azimuth motor.....	38
Figure 2.37. (a) Meteorological station, and (b) meteorological station unit.....	39
Figure 2.38. Video cameras, (a) Ultrak KC550xCP, and (b) SONY SSC-DC393.....	40
Figure 2.39. WISE LAURA interface.....	41
Figure 2.40. FROG LAURA interface.....	41
 Figure 3.1. Instrumentation deployed during WISE 2000 and 2001: (a) L-band polarimetric radiometric (UPC), (b) Ka-band polarimetric radiometer (UMass, only in WISE 2000), (c) L-band polarimetric radiometer (UMass, only in WISE 2000), (d) EMS (buoy 1, ICM CMIMA/CSIC), (e) Aanderaa CMB3280 (buoy 2, ICM CMIMA/CSIC), (f) Datawell wave buoy (buoy 3, LODYC), (g) Clearwater SVP buoy (buoy 4, LODYC), (h) SBE37 Microcat, (i) meteorological station (UPC), (j) stereo-cameras (CETP), (k) video camera (UPC), and (l) IR radiometer (UV).	44
Figure 3.2. (a) Scientific Atlanta pedestal (WISE 2000), (b) new LAURA radiometer pedestal used in WISE 2001, (c) due to the high winds the radiometer was out of control during the November 15 th storm (wind speed > 100 km/h, peak wind speed > 140 km/h at 70 m height).	45
Figure 3.3. Dual polarized L-band radiometer, (a) successfully installation, and (b) test measurements.....	46
Figure 3.4. (a) Ka-band polarimetric radiometer, and (b) positioner internal view.....	47
Figure 3.5. (a) Data acquisition system from the MCV meteorological station and the buoys and, (b) three of the four oceanographic buoys (1,2,4) used in the WISE field experiments.....	48
Figure 3.6. Detail of mooring of Buoy 1.....	49
Figure 3.7. Detail of mooring of Buoy 2.....	51
Figure 3.8. Work Breakdown Structure (WISE 2000).	57
Figure 3.9. WISE 2000 Schedule. KO (kick-off meeting), PM (progress meeting), PCM (pre-campaign meeting), PRM (preliminary results meeting), and DRM (data review meeting).	57
Figure 3.10. Work Breakdown Structure (WISE 2001).	58
Figure 3.11. WISE 2001 Schedule.....	58
Figure 3.12. Casablanca oil rig views, (a) East, and (b) NW, (c) its location, (d) occurrence of strong NW and NE winds in autumn: wind speed recorded during the period of October-December 1992.....	59
Figure 3.13. (a) Occurrence of strong NW and NE winds during the WISE 2000 campaign measured by: the oil rig meteorological station (red), the Coastal Monitoring buoy from ICM (green), and from Quicksat (blue), and (b) occurrence winds during WISE 2001 from November 6 th , 2001 to November 15 th , 2001 when a severe storm destroy the buoy. Data points are averaged every three hours.	60
Figure 3.14. Instruments load and recovery (a) UPC facilities, (b) Sant Carles de la Ràpita harbour, (c) Buoy 3 recovery by the research vessel of ICM "García del Cid" (WISE 2001).	60

Figure 3.15. Casablanca oil rig, (a) North view, radiometers and stereo camera location, (b) Casablanca's helipad limitation for the radiometers cold load calibration (pointing to the sky), (c) upper view, and (d) West lateral view.....	61
Figure 3.16. Upper view of terrace of the radiometers have to be placed, (a) diagram, and (b) picture.....	62
Figure 3.17. (a) Mounting LAURA in the pedestal (WISE 2000), (b) Radiometer is situated in the right point (WISE 2001), and (c) control unit is mounted into the control room.....	62
Figure 3.18. Instrumentation and buoy location during (a) WISE 2000, and (b) WISE 2001.....	63
Figure 3.19. RFI during WISE 2000. Radiometer was pointing to the North ($\phi = 180^\circ$ referred to the South) and $\theta = 44^\circ$).....	65
Figure 3.20. Types of interferences collected during WISE 2000, interferences originated by (a) the walkie-talkies, and (b) saw-tooth interference.....	65
Figure 3.21. Detail of the repair of (a) the video camera cable to acquire data foam, (b) Buoy 1 and, (c) detail of the damage Buoy 2, and ultrasonic anemometer of Buoy 1 (WISE 2001).	65
Figure 3.22. (a) Radiometer cold load calibration, and (b) simulated antenna temperature with contributions from the atmosphere, cosmic and galactic noises.....	66
Figure 3.23. (a) The 90x90 cm microwave absorber in a sealed poly-styrene box with the two temperature sensors, hot load calibration, (b) WISE 2000, $\theta = 105^\circ$, and (c) WISE 2001, $\theta = 0^\circ$	66
 Figure 4.1. Bias between the antenna and the brightness temperature, for LAURA's antenna due to finite beamwidths effects.....	73
Figure 4.2. (a) Sample photogram masked to match the radiometer's beamwidth, and (b) its histogram. The dotted line shows the threshold. Pixels above the threshold are foam-covered.....	75
Figure 4.3. Sample measurements of incidence angle scans at horizontal (left) and vertical polarizations (right) for wind speeds: 1.3 m/s (a-b) and 11.9 m/s (c-d) corresponding to WISE 2000.....	76
Figure 4.4. Brightness temperature dependence vs. U_{10} at H- and V- polarizations at different incidence angles: (a) and (b) 25° , (c) and (d) 35° , (e) and (f) 45° , (g) and (h) 55° , and (i) and (j) 65° . Wind direction relative to the radiometer: Δ = up-wind, ∇ = down-wind, x = cross-wind	77
Figure 4.5. Sensitivity of T_H and T_V to wind speed at 10 m height and associated error bars	78
Figure 4.6. Main oceanographic and meteorological parameters during WISE 2001: (a) Sea surface salinity, (b) sea surface temperature, (c) wind speed referred to 10 m height, (d) atmospheric temperature, (e) significant wave height, and (f) wave period. Until day 305 atmospheric conditions were stable, but after it the sea was significantly warmer than the air (unstable atmosphere).	79
Figure 4.7. Sample measurements of incidence angle scans at horizontal (left) and vertical polarizations (right) for wind speeds: 0.6 m/s (a-b) and 13 m/s (c-d) corresponding to WISE 2001.....	80
Figure 4.8. Derivation of the brightness temperature sensitivity to wind speed: (a) $\Delta T_H(U_{10})$ and (b) $\Delta T_V(U_{10})$ scatter plots, linear fit (solid line) and percentile 50% (dashed lines) as a function of wind speed for incidence angles from 25° to 65° . (c) Derived wind speed (U_{10}) sensitivity as a function of polarization and incidence angle. All data points used.....	81
Figure 4.9. (a) Sensitivity of $T_{H,V}$ to U_{10} derived from Yueh-LODYC model with three different spectra and, (b) WISE 2000-derived brightness temperature sensitivities to U_{10} at H- and V- polarizations, comparison with the Hollinger's measurements and the Yueh-LODYC two-scale model (Durden and Vesey spectrum x2).	82
Figure 4.10. U10 histogram from WISE 2001 field experiment.....	83
Figure 4.11. Predicted wind speed sensitivity using the SSA method and Durden and Vesey spectrum times 2 [36] (a,b) or Elfouhaily et al. spectrum times 2 [35] (c,d) at horizontal (a,c) and vertical (b,d) polarizations.....	83
Figure 4.12. Derived wind speed sensitivity as a function of polarization and incidence angle. Only data points with $U_{10} > 2$ m/s have been retained.....	84
Figure 4.13. Sea state effects-induced brightness temperature (T_B). (Incidence sequence, November 15 th , 2001), (a) instantaneous T_B for H- (blue) and V- (red) polarizations (1 sample = 1second). Fourier transform	

of the instantaneous T_B (solid blue line), filtered spectral density power (dashed red line), (b) H-, (c) V-channel, (d) instantaneous T_B normalized power spectral density (H-polarization dashed blue line, V-polarization solid red line), and (e) variance spectrum measured by the Waverider (Buoy 3), (slopes: solid red line, heights: dashed blue line).....	85
Figure 4.14. Instantaneous T_B normalized power spectral densities (NSDP), (H-polarization dashed blue line, V-polarization solid red line). Radiometer was pointed at to different azimuth angles, (a) $\phi = 260^\circ$ N, (b) $\phi = 320^\circ$ N, (c) variance spectrum measured by the Waverider (Buoy 3) (slopes: solid red line, heights: dashed blue line), and (d) inter-comparison of the NSDP (H-polarization dashed blue line, V-polarization solid red line) and the spectrum height variances measured from Buoy 3 (solid green line). In Table 4.3 the three most probable wave periods (T_1 , T_2 and T_3) are shown. (Large value of T_1 could be due to the swell effect).....	86
Figure 4.15. Derivation of the brightness temperature standard deviation sensitivity to wind speed: (a) H-polarization and b) V-polarization scatter plots, linear fit (solid line) and percentile 50% (dashed lines) as a function of wind speed for incidence angles from 25° to 65° . c) Derived wind speed sensitivity as a function of polarization and incidence angle. All data points used.	87
Figure 4.16. Sample measurements of azimuth scans at horizontal (left) and vertical (right) polarizations for three different wind speeds and incidence angles: (a-b) $\theta = 25^\circ$, $U_{10} = 2.7$ m/s, (c-d) $\theta = 45^\circ$, $U_{10} = 2.8$ m/s, and (e-f) $\theta = 35^\circ$, $U_{10} = 10.9$ m/s.....	88
Figure 4.17. Views of the sea from the 32 m deck during the storm on November 15 th , 2001: a) North-West, b) West.....	89
Figure 4.18. Series of samples acquired during an azimuth scan at 45° incidence angle. November 10 th , 2001, 19 h.....	90
Figure 4.19. Series of samples acquired during an azimuth scan at 55° incidence angle. November 10 th , 2001, 20 h.....	90
Figure 4.20. Foam experiments, (a) emissivity foam measurements (FROG) and, (b) foam distribution over the waves experiment (UPC facilities).....	91
Figure 4.21. Examples of foam formations, (a) Whitecaps, and (b) foam streaks (South Hampton, Alex Smith).....	92
Figure 4.22. Values of the bubble persistence average time (τ_{foam}) as function of breaker wavelength (T_{break}) for three values of the parameter: $a = 0.4$, $a = 0.8$ and $a = 2$, [27].	92
Figure 4.23. (a) Picture of a cross-section through a multi-layer honeycomb foam structure generated in the laboratory [45], and (b) spherical water coated bubble: r is the outer radius, δ is the water-coating thickness, and ϵ_a and ϵ_w are the dielectric permittivity of air and water respectively.	93
Figure 4.24. Foam coverage as a function of the wind speed, (a) WISE 2000's data samples, and (b) static semi-empirical models.....	94
Figure 4.25. WISE 2001's foam coverage as a function of the wind speed (all data samples).....	95
Figure 4.26. Iteration process to get a relation between ΔT_B and foam coverage following a straight line fitted (solid line). 50% confidence levels (dotted line). 1 st iteration for (a) H-channel, (b) V-channel, 4 th iteration for (c) H-channel, (d) V-channel.....	96
Figure 4.27. Brightness temperature induced as a function of the incidence angle for a complete foam-covered spot radiometer. ($F=100\%$).....	97
Figure 4.28. Brightness temperature induced as a function of WISE 2001, $F(U_{10})$, (a) $\theta = 30^\circ$, and (b) $\theta = 50^\circ$	97
Figure 4.29. Brightness temperature induced by foam at 1.4 GHz as function of wind speed for three incidence angles: 0° , 30° and 50° solid curve: V- polarization, dashed curve: H- polarization.	98
Figure 4.30. (a) Removed of foam samples less than 5% of the maximum peak, and (b) mean time between foam generation peaks and standard deviation.....	99
Figure 4.31. Typical patch of foam disappearing over the sea.	99
Figure 4.32. Foam extinction corresponding to eight sequences.....	99
Figure 5.1. (a) Rain generator, and (b) water surface roughed by rain.....	102
Figure 5.2. (a) Foam coverage video camera, and (b) array of air diffusers to create foam.....	103

Figure 5.3. (a) Ultrak video camera inside of a periscope to acquire foam vertical profile images, (b) foam vertical profile acquired during FROG 2003 field experiment, and (c) separation of the foam layer.....	104
Figure 5.4. (a) Brass bars used to measure the water surface roughness, (b) array of golden electrodes to obtain the air-water fraction content, water surface roughness and conductivity meter unit, (c) top view, and (d) front view.....	104
Figure 5.5. Circuits schematic: (a) water roughness and, (b) air-water fraction meter.	105
Figure 5.6. (a) temperature sensor, and (b) datalogger temperature sensor.....	106
Figure 5.7. FROG breakdown structure	108
Figure 5.8. FROG 2003 scheduling	108
Figure 5.9. (a) IRTA facilities, (b) IRTA situation, (c) pool, (d) IRTA facilities plane, (e) container room, and (f) visual description of the set-up.	109
Figure 5.10. Picture of the instruments deployment.....	110
Figure 5.11. (a) Water stopcock, (b) air circuit and its air stopcock, and (c) air escape tube and its air stopcock....	111
Figure 5.12. (a) Radiometer pointing to the hot load, and (b) pointing to the foaming pool.....	114
Figure 5.13. Sample snapshot to determine the foam coverage (FROG field experiment), (a) original image, and (b) processed image, (foam fraction: 69.8 %).	115
Figure 5.14. Void fraction beneath the foam layer measurement, (a), (b) experimental set-up, (c) to (e): conductivity meter.....	116
Figure 5.15. Rain generator mounted at 13 m.	117
 Figure 6.1. Geometrical configuration for thermal emission from foam covered ocean. The foam layer is region 1 and it is absorptive. Region 2 is air bubbles embedded in sea water and it is absorptive [25].	124
Figure 6.2. Measured emissivity (squares, triangles, and circles) at L-band at H- and V- polarizations at different salinity concentrations. Solid lines represent the specular sea surface model at the same salinities.	125
Figure 6.3. Laura radiometric raw data. H- and V- polarization: foam patch (blue/red solid line), foam-free patch (blue/red dotted line), (a) SSS = 33.21 psu, (b) SSS = 37.33 psu. L-band emissivity at H- and V- polarization: foam patch (blue/red solid line), foam-free patch (blue/red dashed line), specular water surface theoretical model (blue/red triangles/circles) (c) SSS = 33.21 psu, mean foam 86.4% (green line), and (d) SSS = 37.33 psu, mean foam 69.7% (green line).	127
Figure 6.4. Foam vertical profiles at different salinities: (a) 0 psu, (b) 5 psu, (c) 10 psu, (d) 15 psu, (e) 20 psu, (f) 25 psu, (g) 30 psu, (h) 37 psu, and (i) natural sea surface bubbles (photograph acquired in the Gran Canaria coast, reference size= 0.50 € coin, radius = 12 mm).	128
Figure 6.5. Distribution of bubbles radii at different salinities: (a) 0 psu, (b) 5 psu, (c) 10 psu, (d) 15 psu, (e) 20 psu, (f) 25 psu, (g) 30 psu, and (h) 34 psu.	129
Figure 6.6. (a) Distribution of the bubbles radii from Gran Canaria coast, and (b) bubbles radii from Gran Canaria coast/gamma distribution (red/blue and solid/dashed line).....	130
Figure 6.7. (a) Different layers of a foam vertical profile, and (b) separation of the foam layer.	130
Figure 6.8. Three different foam vertical profiles: a) fresh water, b) SSS = 20 psu, and c) SSS = 37 psu.	131
Figure 6.9. Air-Water content (f_a) time sequence for every electrode a) SSS = 0 psu (15 electrodes, the top electrode was air), and b) SSS = 37 psu (16 electrodes).	131
Figure 6.10. Air-Water fraction (f_a) mean value for every electrode at SSS = 0 to 34 psu. Each parallel golden electrode (3 mm x 4 mm, total 16) is separated 2 mm to the other. Element number 16 is located over the surface and hence the air-water ratio is 100 %.	132
Figure 6.11. Induced emissivity (@100%) foam per mm at H- and V- polarizations as a function of the SSS and θ . (a) Measured data points (H- polarization), (b) same as Figure 6.11a, low pass filtered, (c) measured data points (V- polarization), and (d) same as Figure 6.11c low pass filtered.	133
Figure 6.12. Foam-induced emissivity vs. incidence angle. Measured data points (H- (triangles, blue) / V- (circles, red)) polarizations, and their corresponding fits (solid line), (H (blue) / V (red)) polarizations.	134

Figure 6.13. Values of κ that minimize the measure sequences and the theoretical model [52] at (a) 5 psu, (b) 15 psu, and (c) 30 psu.....	135
Figure 6.14. Emissivities at H- (blue) and V- (red) polarizations for different salinities. The dashed lines indicate foam-free conditions. The solid line marked with circles indicates the measures taken during FROG campaign and the solid line marked with triangles the theoretical model taken into account some measured parameters: thickness, bubbles radii and f_a , $\delta = 10\mu\text{m}$, and the optimum κ value after fitting the emissivity measures and the theoretical model.	136
Figure 6.15. (a) T_B raw data (mV) with/without rainfall presence (solid line/dotted line) at the H- and V- polarizations for $\theta_i = 25^\circ$ to 50° , and (b) emissivity measured at H- (blue) and V- polarization (red) versus the incidence angle taking into account rainfall (solid line), free-rain (dotted line), and the specular water surface theoretical model (blue/red triangles/circles).	137
Figure 6.16. (a) Temporal data sequence associated to the roughness water surface, (b) slow oscillation due to the dynamic behavior of the water inside the pool, (c) normalized power spectral density vs. frequency of Figure 6.16a, (d) normalized power spectral density vs. wave number of Figure 6.16a.	138
Figure 6.17. T_B change due to the presence of rain computed with SSA model (a) H-, and (b) V- polarization [55].	138
Figure 6.18. Rain-induced emissivity at H- (blue, squares) and V- (red, circles) polarizations. Measurements are fitted by a polynomial of degree 2, excluding the 45° point. Rain rate is scaled to 160 mm/h.	139
Figure 6.19. Theoretically emissivity variation at nadir vs the oil slicks thickness at three different frequencies applying DMRT/QCA (Dense Media Radiative Transfer theory/Quasy Crystalline Approximation) [25].	139
Figure 6.20. Measured (solid) vs theoretical (dashed) emissivity at H- polarization (blue) and V- polarization (red).	140

List of tables

Table 2.1. Isolators characterization at $f_0 = 1.4135$ GHz.....	15
Table 2.2. Control logic. Function table.....	17
Table 2.3. Specifications of LNA stubs.	18
Table 2.4. RF band pass filter insertion and return loss at $f_0 = 1.4135$ GHz	19
Table 2.5. Analogical or software temperature control (HARD/ SOFT). Function table.....	35
Table 2.6. Empirical PID constants.....	36
 Table 3.1. Summary of key measurements and data products.....	¡Error! Marcador no definido.
 Table 4.1. Number of data points for each incidence angle and polarization in WISE 2000.	78
Table 4.2. Number of data points for each incidence angle and polarization in WISE 2000.	81
Table 4.3. Representative three most probable wave periods (T1, T2 and T3) from Figure 4.14 d. The large value of T1 may be due to the swell effect.	86
Table 4.4. Computed peak-to-peak azimuth modulation of the brightness temperature for different wind speeds using the SSA method and Elfouhaily et al. sea spectrum. Other parameters: SSS = 38 psu, SST = 20°C.	91
 Table 5.1. Times in which the salt and fresh pipes have to be open, to achieve the required SSS.....	111
 Table 6.1. Foam emissivity at H- and V- polarizations.....	126
Table 6.2. Foam-induced emissivity per mm at H- and V- polarizations SSS = 37.3 psu.....	134
Table 6.3. Estimated Stickiness factor κ , fitting the measures to the theoretical model.....	135
Table 6.4. Emissivity vs θ , polarization and presence or absence of rain.	137
Table 6.5. Brightness temperature change due to the presence of rainfall scaled to 160 mm/h.	139

Appendix 1. Links to the devices datasheets (12/June/2004)

74HC4060 (BF frequency generator)

<http://www.philipslogic.com/products/hc/pdf/74hc4060.pdf>

AD767 12 bits DAC

http://www.analog.com/UploadedFiles/Data_Sheets/489657162ad767.pdf

AD536A (rms to dc converter)

<http://www.chipcatalog.com/Analog/AD536A.htm>

BP2G (power splitter)

<http://www.minicircuits.com/dg03-114.pdf>

CD4066

<http://www.ee.washington.edu/stores/DataSheets/cd4000/cd4066.pdf>

DS34C86T (current to voltage converter)

<http://cache.national.com/ds/DS/DS34C86T.pdf>

DS34C87T (voltage to current converter)

<http://cache.national.com/ds/DS/DS34C87T.pdf>

IL300 (optocoupler)

http://www.infineon.com/cmc_upload/0/000/008/434/IL300.pdf

INA114 (amp. de instrumentación)

<http://cfa-www.harvard.edu/~thunter/datasheets/INA114.pdf>

LM35

<http://cache.national.com/ds/LM/LM35.pdf>

MACOM's MA4CS102E (diodo detector diferencial)

<http://www.macom.com/data/datasheet/MA4E2054.pdf>

MAR-6 (power amplifier)

<http://www.gamma.pl/technical/minicirc/monamp2.pdf>

MAX238(TTL to RS232 converter)

<http://pdfserv.maxim-ic.com/en/ds/MAX220-MAX249.pdf>

MAX2102 (down-convert)

<http://pdfserv.maxim-ic.com/en/ds/MAX2102EVKIT.pdf>

MAX2640 (LNA)

<http://pdfserv.maxim-ic.com/en/ds/MAX2640-MAX2641.pdf>

MAX915 (comparator)

<http://www.nalanda.nitc.ac.in/industry/datasheets/maxim/PDF/1217.pdf>

NE5561

<http://noel.feld.cvut.cz/semi/phillips/acrobat/5036.pdf>

NE592 (video amplifier)

<http://www.oselectronics.com/downloads/ne592.pdf>

OP37 (amplificador operacional)

http://www.analog.com/Analog_Root/productPage/productHome/0,2121,OP37,00.html

Pico-ADC-12 and Pico-ADC-16 (analogic to digital converter)

www.picotech.com

RSW-2-25p (switches)

<http://www.minicircuits.com/dq03-216.pdf>

STP11NB40

<http://www.mouser.com/catalog/618/319.pdf>

TS924 (operational amplifier)

http://www.jarkad.cz/katalog_listy/t/ts924.pdf

UMA1021M (Divisor programable del PLL)

<http://www.semiconductors.philips.com/pip/UMA1021M.html>

XR-2206

<http://www.avaye.com/electronics/datasheets/timers/XR2206v103.pdf>

Appendix 2. WISE (*Wind and Salinity Experiment*) 2000 and 2001 Instrumentation Technical documentation

- **Sea-Bird 37-SM (MicroCAT) characteristics:**

(Data provided by Sea-Bird Electronics)

The SBE 37-SM is a conductivity and temperature recorder, with internal power supply and memory for data recording. It has a RS232C serial interface and it can be programmed to give sampling rates between 10 seconds and 9.1 hours. The system uses a 24-bit A/D converter to digitise the temperature sensor voltage. The sensor is an ultra-stable aged thermistor and is referred to a VISHAY reference resistor.

PARAMETER CHARACTERISTICS

	Temperature °C	Conductivity (S/m) *
Range	-5 to +35	0 to 7
Accuracy (1)	0.002	0.0003
Stability (2)	0.0002	0.0003
Resolution	0.0001	0.00001
Calibration (3)	+1 to 32	0 to 6

Notes:

* 1 S/m = 10 mS/cm

(1) Initial accuracy when delivered from the factory.

(2) Stability per month

(3) Range of calibration reference data.

The RMS deviation on the salinity calculation from conductivity and temperature is 0.002 psu. The time base is a TCXO of ± 5 ppm vs. temperature (in the range of -5 to +30 °C), with a ± 2 ppm per year ageing, equivalent to ± 2.6 minutes per year. The memory capacity, expressed as number of samples, of the SBE 37-SM MicroCAT, is 410.000 samples (C and T only). For C, T and time, the capacity is 225.000 samples. At a rate of 0.5 sample per minute 410.000 samples, it means 569.4 days of operation (19 months). At the same sampling rate 225.000 samples, it means 312.5 days of operation (10.4 months). Each full power pack is capable to endure 175.000 samples (4 months).

The battery power pack is made of six 9 V lithium batteries, having a total of 6 Ah charge.

- **Salinometer Guildline Autosal characteristics:**

The salinometer that was used is the Model 8400B. This instrument measures the conductivity and the temperature of a sample comparing from a reference water. This reference water has a salinity of 35.0000 psu. The technical characteristics of the instrument are the following:

Accuracy	0.002 psu
Resolution	0.0002 psu
Stability on temperature	0.001°C/day

- USONIC Ultrasonic Anemometer

Wind speed:

Range: 0-60 m/s

Resolution: 0.05 m/s

Accuracy: ± 0.1 m/s (0-5 m/s)

< 1.5% (5-60 m/s)

- Wind direction:

Range: 0° - 360°

Resolution: 1°

Accuracy: < $\pm 3^\circ$

- Temperature: Range: -30° ... $+60^\circ$

Resolution: 0.1 $^\circ$ C

Accuracy: ± 1 $^\circ$ C

- AANDERAA CMB 3280 Coastal Monitoring Buoy characteristics

Reference reading: 413

Sensors:

Wind Speed

Type: three-cup rotor.

Method of measurement: Average over the past measured interval

Range: 0.4 to 76 m/s

Resolution: 0.0746 m/s

Accuracy: ± 2 %

Wind Direction (Buoy orientation sensor)

Type: Direct Earth magnetic field measured by a Hall effect compass.

Method of measurement: Average over the past measured interval.

Range: 0 to 360° referred to magnetic North

Resolution: 0.352°

Accuracy: ± 5°

Air Temperature

Type: Platinum PTC resistor in a radiation screened housing.

Method of measurement: Resistor bridge

Time constant (63 %): 6 minutes

Range: -8 to 41° C

Resolution: 0.048° C

Accuracy: ± 0.1° C

Solar Radiation

Type: Pyranometer

Range: 0 - 2000 W/m²

Resolution: 0.4 W/m²

Accuracy: ± 20 W/m²

Relative Humidity Sensor

Type: Capacitive film sensor, in a radiation screened housing.

WISE 2000 Experiment Plan, v 2.0, 20/07/00 52

Method of measurement: Frequency of an oscillator capacitively tuned. Digital output.

Time constant: 1.5 minutes

Range: 0 to 100 %

Resolution: 0.1 %

Accuracy: ± 3 %

Wave Height

The significant wave height measured as the mean of the highest third of all the waves during the sampling interval.

Type: silicon accelerometer, mounted on a pendulum. Microprocessor controlled, measured each 200 ms and averaged.

Range: 0 to 10 meters (for wave periods of 3 to 8 seconds).

Accuracy: $\pm 10\%$ or ± 0.2 meters (whichever is greater).

Wave Period

Type: Calculated in the same sensor with wave height.

Range: 1 to 30 seconds

Accuracy: $\pm 10\%$

- **AANDERAA RCM9 current meter:**

Current speed

Type: Doppler sensor. Vector averaging at 600 pings during sampling interval.

Includes one tilt sensor for current speed and direction correction

Acoustic Frequency: 2 MHz

Beam angle: $\pm 1^\circ$ (Main lobe)

Range: 0 to 500 cm/s

Accuracy: 2 cm/s or $\pm 2\%$ of actual speed.

Current Direction

Type: Uses the same Doppler sensor used for current speed.

Range 0 to 360° respect magnetic North.

Accuracy: $\pm 5^\circ$ for 0 to 15° tilt of the buoy

$\pm 7.5^\circ$ for $15 - 35^\circ$ tilt of the buoy

Water Temperature

Type: Platinum sensor located on the Doppler current sensor.

Range: -8 to 41° C

Accuracy: $\pm 0.1^\circ$ C

Appendix 3. Instruments specifications

- **SONY SSC-DC393**

Specifications

	SSC-DC193	SSC-DC393
Image device	1/3 type Interline Transfer Super HAD CCD	1/3 type Interline Transfer Exwave HAD CCD
Picture elements (H x V)	510 x 492	768 x 494
Sensing area	1/3" format (4.8 x 3.6 mm)	
Signal system	NTSC standard	
Sync. System	INT/LL	
Horizontal resolution	330 TV lines	480 TV lines
Lens mount	CS	
Minimum illumination	0.3 lx at F1.2 (30 IRE, AGC ON, Turbo mode) 0.6 lx at F1.2 (50 IRE, AGC ON, Turbo mode) 3.0 lx at F1.2 (100 IRE, AGC ON, Turbo mode)	0.35 lx at F1.2 (30 IRE, AGC ON, Turbo mode) 0.7 lx at F1.2 (50 IRE, AGC ON, Turbo mode) 3.5 lx at F1.2 (100 IRE, AGC ON, Turbo mode)
AGC	ON/OFF switchable	
CCD IRIS	ON/OFF (switchable), 1/60 to 1/100,000 s	
White Balance (WB)	ATW	
Back-Light Compensation (BLC)	ON/OFF switchable	
S/N ratio	More than 50 dB (AGC OFF, Weight ON)	
Video out	BNC, 1.0 Vp-p, 75 Ω, sync. negative	
Operating temperature	-10°C to 50°C (14°F to 122°F)	
Storage temperature	-40°C to 60°C (-40°F to 140°F)	
Power requirements	AC 24 V ±10%, 60Hz or DC 12 V ±10%	
Power consumption	3.5 W	3.7 W
Auto iris lens	DC/video servo switchable	
Weight	13 oz (360 g)	
Dimensions (W x H x D)	2 3/8 x 2 1/4 x 4 3/4 inches (60 x 54 x 120 mm)	
Supplied accessories	Lens mount cap (1) Operating instruction (1)	

- **Ademco high resolution Lens**

FEATURES:	PART NUMBERS – AUTO IRIS LENSES				
	ALD02813L	ALD0412S	ALD0812S	ALD3V813S	ALD5V5018L
Image Format	3"	1/3"	1/3"	1/3"	1/3"
Focal Length	2.8mm	4mm	8mm	3-8mm	5-50mm
Iris Range	F1.3-T360	F1.2-T360	F1.2-T360	F1.3-T360	F1.8-T360
Focus Range	.1m to infinity	.1m to infinity	.1m to infinity	.3m to infinity 1m (@tele)	.3m (@wide)
Back Focus distance	8.11mm	8.62mm	8.81mm	8.07mm (in air) 11.08 (@tele)	9.70mm (@wide)
Weight	40g	40g	40g	70g	225g
Lens Mount	CS	CS	CS	CS	CS
Iris Control	4-pin DC Control	4-pin DC Control	4-pin DC Control	4-pin DC Control	4-pin DC Control
Focus Control	Manual	Manual	Manual	Manual	Manual
Iris Control cable	230mm	100mm	100mm	100mm	100mm
Dimensions (DxLxW)	32x35x44mm	32x35x44mm	32x35x44mm	41x50x48mm	54x86x54mm

- **Ultrak KC550xCP**

Power

- Power Source 12V DC/24V AC +/- 10% or
230VAC +/- 10%, 50 Hz +/- 1%
- Power Consumption Max. 3.6 Watts
- Power Indicator Green LED

Sensor Information and General

- Processing Technology Sony DSP
- Image Sensor 1/3" interline transfer CCD(sony chip set)
- Picture Element 600(H) x 582(V)
- Chip Size 6.0mm(H) x 4.96mm(V)
- Unit Cell Size 9.8um(H) x 6.3um(V)
- Scanning System 2:1 interlace
- Scanning Frequency 15.625KHz(H), 60Hz(V)
- Sync System Line Lock
- Vert Phase Adjust Range 0 deg. to 360 deg
- Electronic Shutter 1/60 ~ 1/100,000 sec.
- Operating Temperature / Humidity -10°C ~ +50°C (14°F ~ 122°F) / <96% (Non-condensing)

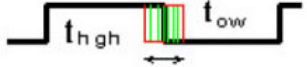
Connector and Mechanical

- Video Output BNC Connector
- Power Input 3-pin Terminal Block or Power Cord
- AI/DC Output 4-pin mini din jack
(Standard Connection)
- Lens Mount C/CS(selected through back focus)
- Back Focus & C/CS Adjust Built in Back Focus Cam with Thumb Wheel Adjust
(Range:-1.5mm to +6.5mm)
- B/F & C/CS Lock Phillips Tension Screw
- Mounting Hole 1/4" UNC Top and Bottom
- External Dimensions 62(W) x 54(H) x 140(D)
- Weight 290g (~10.2 oz)

Video

- Signal Format PAL 625 Lines
- Resolution 330 TV Lines
- Minimum Illumination 0.8 Lux(F1.2)
- Video Output 1.0Vp-p, 75 ohm unbalanced
- Video Iris Output 650mV at video out 1.0 Vp-p
- S/N Ratio 46 dB (AGC Off)
- BLC Size 40% center
- Sync Level 40 IRE
- White Clip 120 IRE
- Auto/Man Shutter Control (E.S.) Auto(On), Man(Off) (Dip Switch)
1/60(1/50), 1/100(F.F.), 1/250, 1/500, 1/1000,
1/4000, 1/10,000, 1/100,000(Default 1/60)
- Manual Shutter Control AI/DC (Dip Switch)
- Auto Iris ON/OFF (Dip Switch)
- BLC On(0.45)/Off(1) (Dip Switch)
- Gamma On/Off (Dip Switch)
- AGC Adjustable (Tact Switch Up/Down)
- Vert Phase Adjust Adjustable (POT)
- DC Iris Level Adjust Auto (3200K ~ 8000K), 3200K,
4200K, 6300K (2 Dip Switches)
- White Balance

- Seika clinometer

Type	N2	N3	N4
Measuring range	$\pm 10^\circ$	$\pm 30^\circ$	$\pm 70^\circ$
Resolution	< 0.002°	< 0.005°	0.01°
Dimensions - with Mounting Ring	.976" (24.8mm) dia. X .46" (11.7mm) h 1.46" (37mm) dia. X .46" (11.7 mm) h		
Max. Non-linearity	<0.2% from measuring value!		
Transverse Sensitivity	<1% at 30° tilt		
Response time	< 0.3 Sec.		
Power Supply U_{bN} (Regulated)	5 Volt		
Min ... Max. Supply U_{bz}	3 ... 6 Volt		
Current consumption $U_b=5$ Volt	Approx. 1mA		
Protection degree	IP65		
Operating temperature	-40 to +85°C		
Storage temperature	-45 to +90°C		
Weight (without cable and mounting ring)	Approx. .653 ounces (18.5 grams)		
Cabling	Standard: 3 highly flexible, individually shielded wires; shielding .039" (\varnothing 1.0mm) x 7.09" (180mm) l Optional: Shielded cable .083" (\varnothing 2.1mm) x 19.69" (0.5m) l		
Values for analog DC output model at $U_{bN}=5$Volt			
Sensitivity	Approx. 12mV/°	Approx. 5mV/°	Approx. 3.2mV/°
Temperature drift of sensitivity	-0.17%/°C	< -0.12%/°C	
Temperature drift of zero	< ± 0.05 mV/°C	< ± 0.025 mV/°C	
Zero offset at $Ub=5$ V	2.5 \pm 0.1 Volt - generally: 0.5Ub \pm 4%		
Output Impedance	10kΩ		
Values for duty cycle for digital pulse width modulated output model at $U_{bN}=5$Volt			
			
Sensitivity $dt_{(E)}/(t_{high}+t_{low})$	Approx. $76 \cdot 10^{-3}$ /°	Approx. $33 \cdot 10^{-3}$ /°	Approx. $20 \cdot 10^{-3}$ /°
Temperature drift of sensitivity	-0.17%/°C	< -0.12%/°C	
Temperature drift of zero	< $\pm 1.6 \cdot 10^{-4}$ FS/°C	< $\pm 8 \cdot 10^{-5}$ FS/°C	
Middle initial point t_{high}/t_{low}	1 \pm 4%		
Output frequency	Approx. 20Hz to approx. 1MHz (optional)		

